

Article

# The Effect of Cu and Ga Doped ZnIn<sub>2</sub>S<sub>4</sub> under Visible Light on the High Generation of H<sub>2</sub> Production

Ikki Tateishi <sup>1,\*</sup>, Mai Furukawa <sup>2</sup>, Hideyuki Katsumata <sup>2</sup>  and Satoshi Kaneco <sup>1,2</sup> 

<sup>1</sup> Global Environment Center for Education & Research, Mie University, Mie 514-8507, Japan; kaneco@chem.mie-u.ac.jp

<sup>2</sup> Department of Chemistry for Materials, Graduate School of Engineering, Mie University, Mie 514-8507, Japan; maif@chem.mie-u.ac.jp (M.F.); hidek@chem.mie-u.ac.jp (H.K.)

\* Correspondence: tateishi@gecer.mie-u.ac.jp; Tel.: +81-59-231-9647

Received: 28 June 2019; Accepted: 25 September 2019; Published: 29 September 2019



**Abstract:** A Cu<sup>+</sup> and Ga<sup>3+</sup> co-doped ZnIn<sub>2</sub>S<sub>4</sub> photocatalyst (Zn<sub>(1-2x)</sub>(CuGa)<sub>x</sub>In<sub>2</sub>S<sub>4</sub>) with controlled band gap was prepared via a simple one-step solvothermal method. Zn<sub>(1-2x)</sub>(CuGa)<sub>x</sub>In<sub>2</sub>S<sub>4</sub> acted as an efficient photocatalyst for H<sub>2</sub> evolution under visible light irradiation ( $\lambda > 420$  nm; 4500  $\mu$ W/cm<sup>2</sup>). The effects of the (Cu and Ga)/Zn molar ratios of Zn<sub>(1-2x)</sub>(CuGa)<sub>x</sub>In<sub>2</sub>S<sub>4</sub> on the crystal structure (hexagonal structure), morphology (microsphere-like flower), optical property (light harvesting activity and charge hole separation ability), and photocatalytic activity have been investigated in detail. The maximum H<sub>2</sub> evolution rate (1650  $\mu$ mol·h<sup>-1</sup>·g<sup>-1</sup>) was achieved over Zn<sub>0.84</sub>(CuGa)<sub>0.13</sub>In<sub>2</sub>S<sub>4</sub>, showing a 3.3 times higher rate than that of untreated ZnIn<sub>2</sub>S<sub>4</sub>. The bandgap energy of Zn<sub>(1-2x)</sub>(CuGa)<sub>x</sub>In<sub>2</sub>S<sub>4</sub> decreased from 2.67 to 1.90 eV as the amount of doping Cu<sup>+</sup> and Ga<sup>3+</sup> increased.

**Keywords:** photocatalytic hydrogen generation; copper; gallium; ZnIn<sub>2</sub>S<sub>4</sub>

## 1. Introduction

Global energy shortage and the environmental pollution associated with burning fossil fuels have stimulated people's interest in clean and sustainable energy. Photocatalytic hydrogen evolution through water splitting and photocatalytic CO<sub>2</sub> reduction on semiconductor photocatalysts, are of interest due to their intriguing application to converting solar energy to chemical energy [1–6]. Among the two processes, the photocatalytic hydrogen production plays an important role, producing hydrogen for society. Sunlight contains ultraviolet light, visible light, and infrared light, and it is ideal to use all the wavelengths when using sunlight. It is known that the wavelength ranges of light in which the photocatalyst reacts are caused by the size of the band gap of the photocatalyst [7–9]. Metal sulfides have a relatively negative valence band (VB) edge and a narrower band gap derived from sulfide ions than metal oxides. Therefore, photocatalytic activity can be exhibited even with long wavelength light [10–12]. The addition of foreign elements, which is one of the ways to change these factors, greatly affects the characteristics of the catalyst. Specific requirements to improve the activity of the photocatalytic material include efficient light absorption, effective separation of photogenerated charge carriers, and better efficiency to the interface for direct release of hydrogen and/or oxygen from water [13–15]. In efficient light absorption, the size of the band gap formed by the conduction band (CB) and the valence band of the semiconductor's photocatalyst is the most important issue [16–18]. In regard to the effective separation of photogenerated charge carriers, many elements, such as defects in the crystal structure and band structure, are involved in a complex manner [19–21]. Sulfide photocatalysts are advantageous for visible light driven photocatalysts because they have narrow band gaps and negative valence bands, due to the S electron orbital, than oxide-based photocatalysts [22–24].

ZnIn<sub>2</sub>S<sub>4</sub> has been reported to have a suitable band gap corresponding to the visible-light absorption region, high photocatalytic activity, and considerable chemical stability for photocatalytic H<sub>2</sub> evolution. However, bare ZnIn<sub>2</sub>S<sub>4</sub> can show inferior performance for photocatalytic hydrogen evolution due to the short lifetime of the photo-induced carriers, and is expected to be further improved for the visible light response [25–27]. In recent years, there have been various studies for improving the photocatalytic activity of ZnIn<sub>2</sub>S<sub>4</sub> [28,29]. Cu species, such as Cu<sup>+</sup> and Cu<sup>2+</sup>, affected the valence band of ZnIn<sub>2</sub>S<sub>4</sub> and constituted an advantageous band structure for photocatalysts [30–32]. It has been found that Ga doping into TiO<sub>2</sub> produces an oxygen vacancy and an incomplete level conduction band, and electron traps enhance the separation of photogenerated electron-hole pairs [33–35]. Additionally, since Zn<sup>2+</sup> (88 pm), Cu<sup>+</sup> (91 pm), and Ga<sup>3+</sup> (76 pm) have relatively similar radii, it is not difficult to replace the Zn<sup>2+</sup> part of ZnIn<sub>2</sub>S<sub>4</sub> with Cu<sup>+</sup> and Ga<sup>3+</sup>. Since the solid solution changes structural, mechanical, optical, and physical properties more dramatically than simple phase mixtures, the properties can be controlled [36]. Ga doping into ZnGa<sub>2</sub>S<sub>4</sub> improved the photocatalytic activity [37]. Since ZnIn<sub>2</sub>S<sub>4</sub> and ZnGa<sub>2</sub>S<sub>4</sub> have a similar chalcopyrite structure, the insertion of Ga into ZnIn<sub>2</sub>S<sub>4</sub> was hypothesized to improve the photocatalytic activity. Therefore, it is reasonable to think that doping Ga into ZnIn<sub>2</sub>S<sub>4</sub> improves the hydrogen generation activity. There are a few reports that ZnIn<sub>2</sub>S<sub>4</sub> is co-doped Cu<sup>+</sup> and Ga<sup>3+</sup>. In this study, we investigated photocatalytic activity, optical properties, and surface morphology of ZnIn<sub>2</sub>S<sub>4</sub> simultaneously co-doped with Ga<sup>3+</sup> and Cu<sup>+</sup>.

## 2. Materials and Methods

### 2.1. Preparation of Photocatalysts

All chemicals were analytical grade and used as received without further purification. Zn<sub>(1–2x)</sub>(CuGa)<sub>x</sub>In<sub>2</sub>S<sub>4</sub> compounds were prepared by a simple hydrothermal method. In total, 3.76 mmol of cetyltrimethylammonium bromide (CTAB) (Wako Pure Chemical Industries, Ltd., Japan), a stoichiometric ratio of ZnSO<sub>4</sub>·7H<sub>2</sub>O (Nacalai Tesque, Inc., Japan), InCl<sub>3</sub>·4H<sub>2</sub>O, CuCl (I), gallium chloride (III), and the excess of thioacetamide (TAA) (Wako Pure Chemical Industries, Ltd., Japan) were dissolved in 50 mL of distilled water. The starting chemical reagents are shown in Table S1. In order to keep Cu monovalent, nitrogen was purged for 10 min to remove dissolved oxygen. The mixed solution was then transferred into a 100 mL Teflon autoclave. The autoclave was sealed and kept at 160 °C for 1 h and cooled to room temperature naturally. After cooling, the product was dried in a vacuum at 40 °C for 4 h and was ground for 30 min. ZnIn<sub>2</sub>S<sub>4</sub> (no doped), Zn<sub>0.87</sub>Cu<sub>0.13</sub>In<sub>2</sub>S<sub>3.935</sub> (only Cu<sup>+</sup> doped), and Zn<sub>0.87</sub>Ga<sub>0.13</sub>In<sub>2</sub>S<sub>4.065</sub> (only Ga<sup>3+</sup> doped) were also prepared by the same method as the reference material. The prepared photocatalysts are shown in the Table S2.

### 2.2. Characterization of Samples

X-ray powder diffraction (XRD) measurements were performed using a Rigaku RINT Ultima-IV diffractometer. That was carried out using Cu radiation at a scan rate of 0.04°/s in a scan range of 10–80°. X-ray photoelectron spectroscopy (XPS) measurements were carried out with a PHI Quantera SXM photoelectron spectrometer using Al K $\alpha$  radiation. To compensate for surface charges effects, binding energies were calibrated using the C1s peak at 284 eV as the reference. Scanning electron microscope (SEM) observations were performed using a Hitachi S-4000 SEM. The transmission electron microscopy (TEM) images were taken on JEOL product JEM1011. The nitrogen adsorption and desorption isotherm and the Brunauer Emmett Teller (BET) specific surface area were measured from BELSORP miniII (MicrotracBEL Corp). The UV–vis diffuse reflectance spectra (DRS) of the photocatalysts were recorded using a Shimadzu UV-2450 spectrophotometer equipped with an integral sphere assembly, using BaSO<sub>4</sub> as a reflectance standard. Photoluminescence (PL) spectra were obtained at an excitation wavelength of 350 nm using a Shimadzu RF-5300PC spectrofluorophotometer. The band gap was calculated from

Equation (1). In addition, valence bands and conduction bands were calculated from XPS results and band gap values.

$$\alpha h\nu = A(h\nu - E_g)^n \quad (1)$$

where  $h$ ,  $\alpha$ ,  $\nu$ ,  $A$ , and  $E_g$  represent Planck's constant, optical absorption coefficient, photon frequency, a constant, and the photonic energy band gap; and  $n = 1/2$  for a direct band gap semiconductor.

### 2.3. Photocatalytic Hydrogen Generation

The side-irradiation-type pyrex batch reactor (inner volume: 123 mL) was used for the photocatalytic production of hydrogen from aqueous sulfide solution. A 300 W Xe lamp was used as the light source, and the UV part of the light was removed by a cutoff filter ( $\lambda \geq 420$  nm). In all experiments, 40 mL of solution (pH12) containing 40 mg of catalyst, 0.01  $\mu\text{g}$  Pt/mL of  $\text{H}_2\text{PtCl}_6$ , and 0.25 M  $\text{Na}_2\text{SO}_3$ /0.35 M  $\text{Na}_2\text{S}$  mixed sacrificial agent was added into the reaction cell. The light source was a 4000–4500  $\mu\text{W}/\text{cm}^2$  Xe-lamp, used for 6 h with a cut-off filter ( $\lambda \geq 420$  nm). Nitrogen purged through the system for 30 min before the reaction to remove oxygen. The concentrations of  $\text{H}_2$  were measured with a gas chromatograph (GC). The injection, column, and detector in the GC were 50 °C. A thermal conductivity detector (TCD) was used as the detector. The hydrogen generation experimental conditions are shown in Table 1. In the experiment on the stability of the photocatalyst, one cycle of photocatalytic hydrogen generation was 6 h, and 4 cycles were performed under the same conditions. At the end of each cycle, a nitrogen purge was performed in the reaction vessel to remove residual hydrogen.

**Table 1.** Hydrogen generation experimental conditions.

Photocatalyst	$\text{Zn}_{(1-2x)}(\text{CuGa})_x\text{In}_2\text{S}_4$ ( $x = 0, 0.07, 0.10, 0.13, 0.16, 0.19$ ) $\text{Zn}_{0.87}\text{Cu}_{0.13}\text{In}_2\text{S}_{3.935}$ , $\text{Zn}_{0.87}\text{Ga}_{0.13}\text{In}_2\text{S}_{4.065}$
Cocatalyst	$\text{H}_2\text{PtCl}_6$ (1.0 wt%)
Medium	0.25 M $\text{Na}_2\text{SO}_3$ /0.35 M $\text{Na}_2\text{S}$ 40 mL, (pH 12)
Reactor	Pyrex glass vessel (volume: 123 mL)
Temperature	Room Temperature (25 °C)
Light source	Xenon lamp ( $\lambda \geq 420$ nm, 4500 $\mu\text{W}/\text{cm}^2$ )
Irradiation time	6 h
Analysis	Gas chromatography (TCD)

## 3. Results and Discussion

### 3.1. Structural Characterization

The XRD patterns of  $\text{Zn}_{(1-2x)}(\text{CuGa})_x\text{In}_2\text{S}_4$  are shown in Figure 1. The XRD pattern of  $\text{ZnIn}_2\text{S}_4$  could be indexed as the hexagonal structure (JCPDS number 65-2023). The four diffraction peaks at around 20.8°, 27.5°, 47.2°, and 55.9° could be assigned to the (006), (101), and (110) and (202) planes, respectively [38,39]. The XRD patterns of other composition ratio of  $\text{Zn}_{(1-2x)}(\text{CuGa})_x\text{In}_2\text{S}_4$  also showed the similar results. This XRD patterns were in agreement with those reported in previous studies, which revealed it that  $\text{Zn}_{(1-2x)}(\text{CuGa})_x\text{In}_2\text{S}_4$  is a hexagonal structure and contained almost no impurities of ZnS. The reason for the fact that the Cu and Ga derived peaks were not observed could be due to the very low doping amount. In addition, with respect to the peak of the (006) plane, a slight shift toward the high angle was observed when doping with Cu and Ga. This means it that the interplanar spacing is reduced by doping, suggesting that Cu and Ga may be incorporated into the crystal structure of  $\text{ZnIn}_2\text{S}_4$  and exist as a solid solution. The shift of the peak was observed between  $x = 0$  and 0.13 in the doping amount, and a further shift was not observed when  $x = 0.16$  and 0.19. This result indicates that beyond  $x = 0.13$ , it was not incorporated into the crystal structure of  $\text{ZnIn}_2\text{S}_4$ .

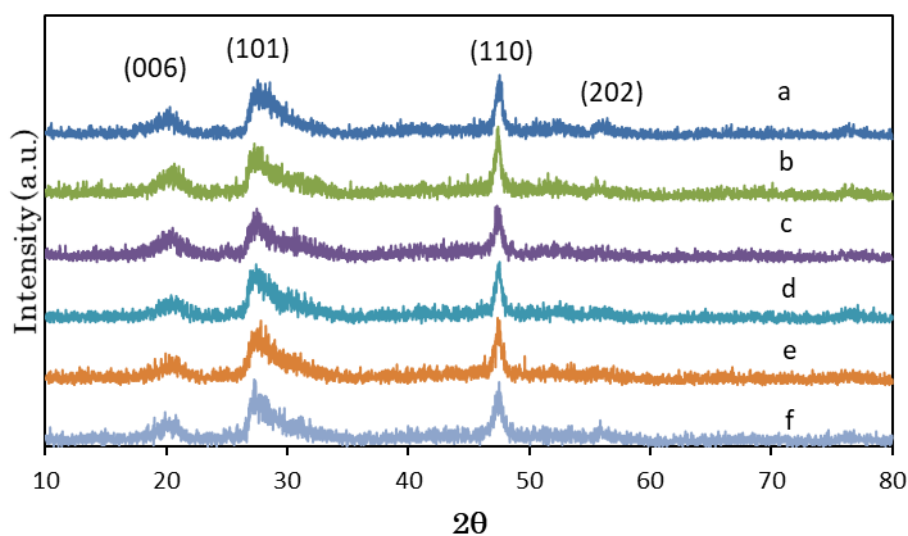


**Figure 1.** XRD patterns of  $Zn_{(1-2x)}(CuGa)_xIn_2S_4$ . (a)  $x = 0$ , (b)  $x = 0.07$ , (c)  $x = 0.10$ , (d)  $x = 0.13$ , (e)  $x = 0.16$ , and (f)  $x = 0.19$ .

The results of XPS measurement for further structural analysis of photocatalysts are shown in Figure S1. The elemental ratios determined from the XPS spectrum are shown in the Table S3. A series of XPS survey spectra matched the reference material  $ZnIn_2S_4$ . This indicates that the impurities are not present, regardless of the doping amounts of Cu and Ga. Furthermore, from the result of elemental ratio analysis of XPS, it was able to be confirmed that the elemental ratio of the prepared catalysts was substantially in agreement with the theoretical ratio. Typical narrow spectra of  $Zn_{(1-2x)}(CuGa)_xIn_2S_4$  are shown in Figure 2. In the XPS spectrum of Zn 2p, two peaks located at Zn 2p<sub>3/2</sub> (1020.4 eV) and Zn 2p<sub>1/2</sub> (1043.6 eV) were observed. Binding energies of 443.7 (In 3d<sub>5/2</sub>) and 451.0 eV (In 3d<sub>3/2</sub>) were observed in the XPS spectrum of In 3d. The peaks of S 2p were at 161.3 (S 2p<sub>3/2</sub>) and 162.6 eV (S 2p<sub>1/2</sub>) [40,41]. In addition, since the peak position of Cu 2p<sub>3/2</sub> was observed only at 932 eV, and Cu 2p<sub>3/2</sub> satellite peak derived from Cu<sup>2+</sup> was not present at 942 eV, it can be seen that Cu was doped in a monovalent state [42,43]. The Ga 2p<sub>1/2</sub> and Ga 2p<sub>3/2</sub> peaks derived from Ga<sup>3+</sup> were located at around 1144 eV and 1117 eV, respectively [44]. These results of XRD and XPS show that the basic structure of  $Zn_{(1-2x)}(CuGa)_xIn_2S_4$  is hexagonal  $ZnIn_2S_4$ , co-doped with Cu<sup>+</sup> and Ga<sup>3+</sup>.

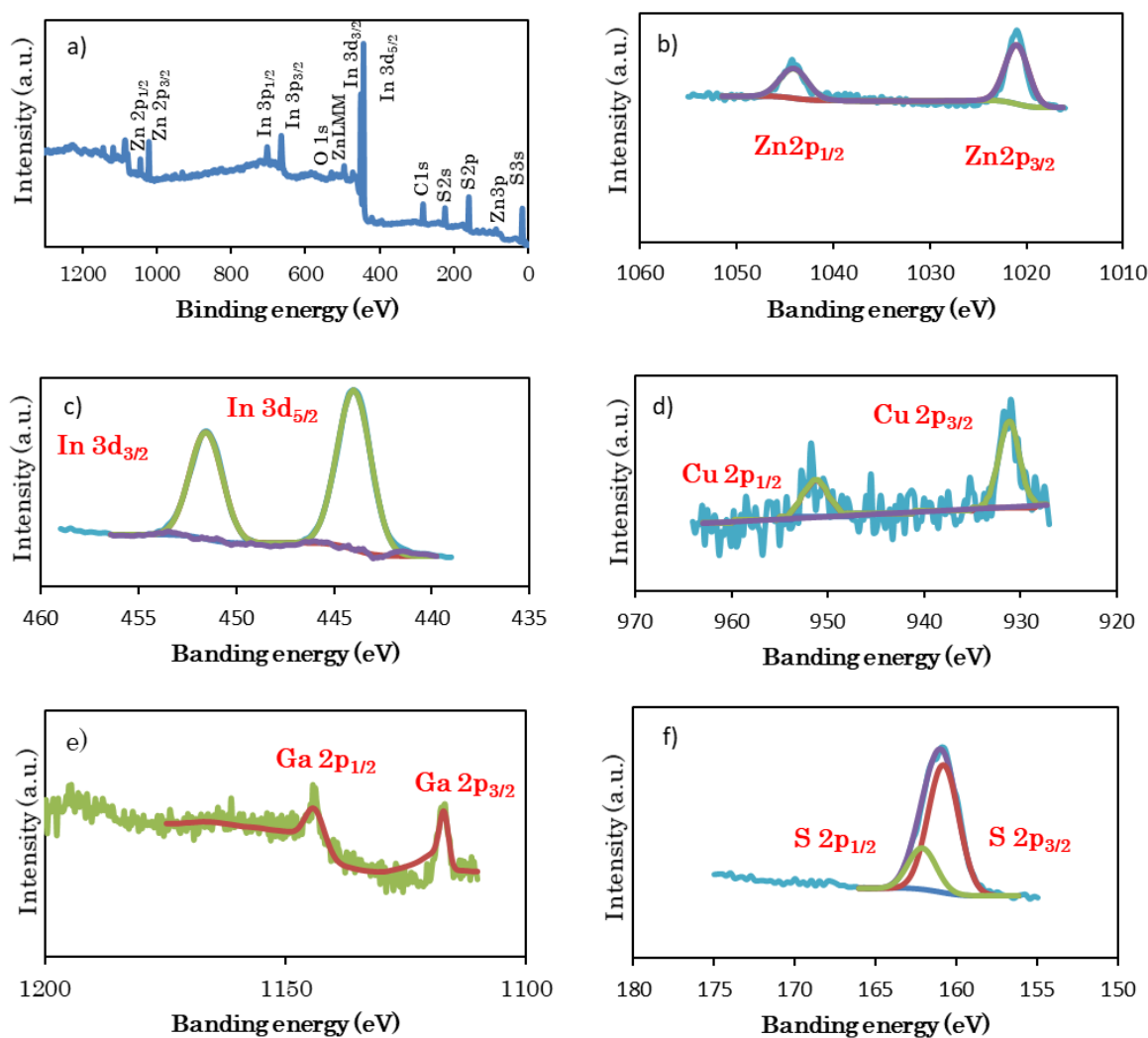


**Figure 2.** XPS narrow and survey spectra of  $\text{Zn}_{0.62}(\text{CuGa})_{0.19}\text{In}_2\text{S}_4$ . (a) survey, (b) Zn, (c) In, (d) Cu, (e) Ga, and (f) S.

### 3.2. Morphological Analysis

In order to investigate the influence of Cu and Ga doping on the characteristic surface morphology of  $\text{Zn}_{(1-2x)}(\text{CuGa})_x\text{In}_2\text{S}_4$ , SEM images of the prepared photocatalysts were observed. The results are shown in Figure 3. In pure  $\text{ZnIn}_2\text{S}_4$ , a microsphere-structure-like flower formed by overlapping of nanosheets was observed [45]. Co-doped with Ga and Cu, the spherical structure was destroyed, and the destruction was promoted as the doping amount increased. The nanosheet structure also collapsed and aggregated as the doping amount of Ga and Cu increased. The shapes of pure  $\text{ZnIn}_2\text{S}_4$  and  $\text{Zn}_{0.62}(\text{CuGa})_{0.19}\text{In}_2\text{S}_4$  were very different.  $\text{Cu}^+$ ,  $\text{Ga}^{3+}$ , and  $\text{ZnIn}_2\text{S}_4$  are not composites; solid solutions may have been formed.

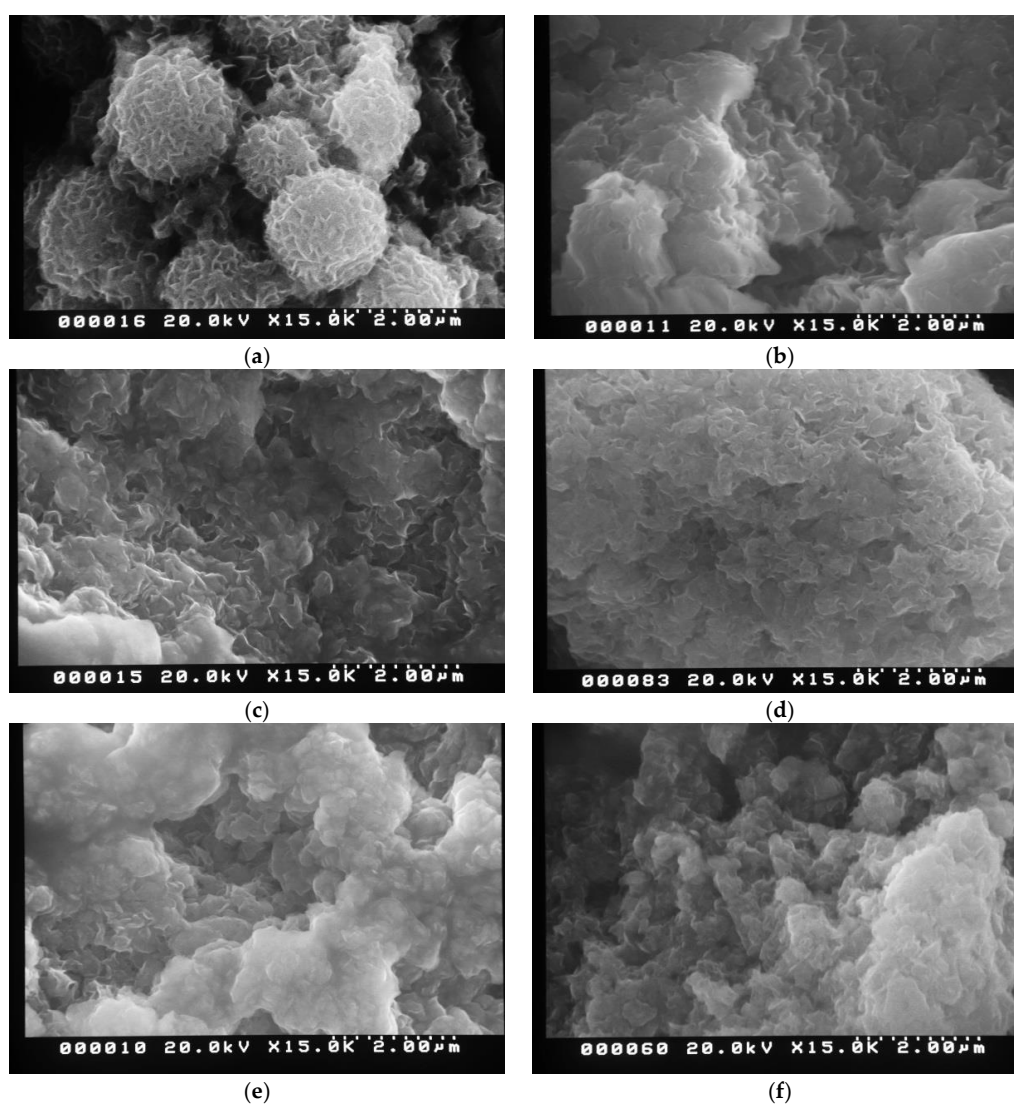


**Figure 3.** SEM images of  $\text{Zn}_{(1-2x)}(\text{CuGa})_x\text{In}_2\text{S}_4$ . (a)  $x = 0$ , (b)  $x = 0.07$ , (c)  $x = 0.10$ , (d)  $x = 0.13$ , (e)  $x = 0.16$ , and (f)  $x = 0.19$ .

The nitrogen adsorption and desorption isotherm and BET specific surface area are shown in Figure S2 and Table S4, respectively. According to the results, co  $\text{Cu}^+$  and  $\text{Ga}^{3+}$  doping increased the specific surface area. The specific surface area of  $\text{Zn}_{0.74}(\text{CuGa})_{0.13}\text{In}_2\text{S}_4$  was six times larger than that of  $\text{ZnIn}_2\text{S}_4$ . This result could be related to the surface morphology observed by SEM.

### 3.3. Optical Analysis

Figure 4 shows the relationship between the doping amount of Cu and Ga to  $\text{ZnIn}_2\text{S}_4$  and the absorption wavelength region of light using the UV-visible diffuse reflectance spectrum. Figure S3 shows the fitting curve of  $(\alpha h\nu)^{1/n}$  versus  $h\nu$ , for various  $\text{Zn}_{(1-2x)}(\text{CuGa})_x\text{In}_2\text{S}_4$  photocatalysts; the curve was best fitted when  $n = \frac{1}{2}$ , meaning that  $\text{Zn}_{(1-2x)}(\text{CuGa})_x\text{In}_2\text{S}_4$  photocatalysts have a direct band gap transition. As shown in the literature, the absorption edge of pure  $\text{ZnIn}_2\text{S}_4$  was 480 nm, and the size of the band gap was 2.67 eV. For  $\text{Zn}_{(1-2x)}(\text{CuGa})_x\text{In}_2\text{S}_4$ , as the doping amount was increased, the absorption edge of photocatalyst was red-shifted, because the 3d orbital derived from  $\text{Cu}^+$  affects the valence band edge of  $\text{ZnIn}_2\text{S}_4$ , and the 4s orbital from  $\text{Ga}^{3+}$  influences the conduction band edge for  $\text{ZnIn}_2\text{S}_4$ . The absorption edge reached about 700 nm when the doping amount was  $x = 0.13$ , but a further increase in the doping amount ( $x = 0.16$  and  $0.19$ ) had scarcely any influence

on the absorption edge. The results could be explained by the same doping amount over  $x = 0.13$ . Additionally, the band gap of  $\text{Zn}_{(1-2x)}(\text{CuGa})_x\text{In}_2\text{S}_4$  similarly decreased as the doping amount of  $\text{Cu}^+$  and  $\text{Ga}^{3+}$  increased. In addition, to evaluate the band structure, the valence band edge measurements for  $\text{ZnIn}_2\text{S}_4$  and  $\text{Zn}_{0.74}(\text{CuGa})_{0.13}\text{In}_2\text{S}_4$  were performed by XPS. From Figure S4, the valence band edge of  $\text{Zn}_{0.74}(\text{CuGa})_{0.13}\text{In}_2\text{S}_4$  is visibly 0.7 V lower than that of  $\text{ZnIn}_2\text{S}_4$ .

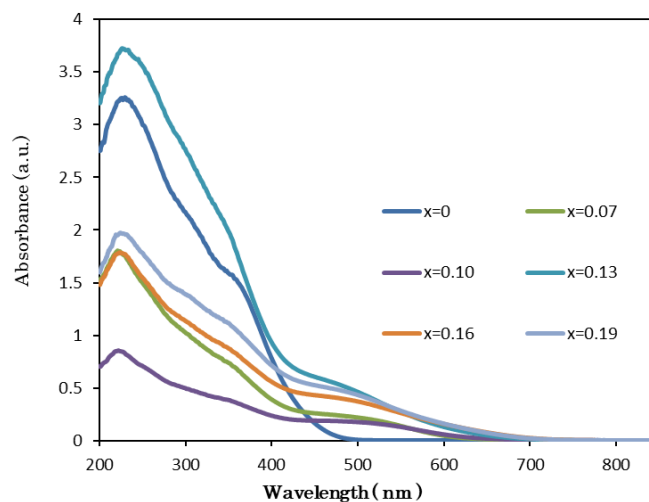


**Figure 4.** UV-visible spectra of  $\text{Zn}_{(1-2x)}(\text{CuGa})_x\text{In}_2\text{S}_4$ .

We investigated the photoluminescence spectra in order to investigate the electron-hole pair separation efficiency due to the doping of Cu and Ga, and the results are shown in the Figure 5. Luminescence in ultraviolet and visible regions was observed in the photoluminescence spectrum. In general, ultraviolet emission is associated with exciton transition and recombination from the conduction band level to the valence band, and visible light emission is mainly associated with intrinsic or extrinsic defects in the catalyst. Both peaks in the spectrum were lowered by increasing the  $\text{Cu}^+$  and  $\text{Ga}^{3+}$  doping. This may be due to the reduction of the recombination rate between the photogenerated holes and the electrons photogenerated in the valence band being trapped in the oxygen vacancies generated in the photocatalyst by doping.

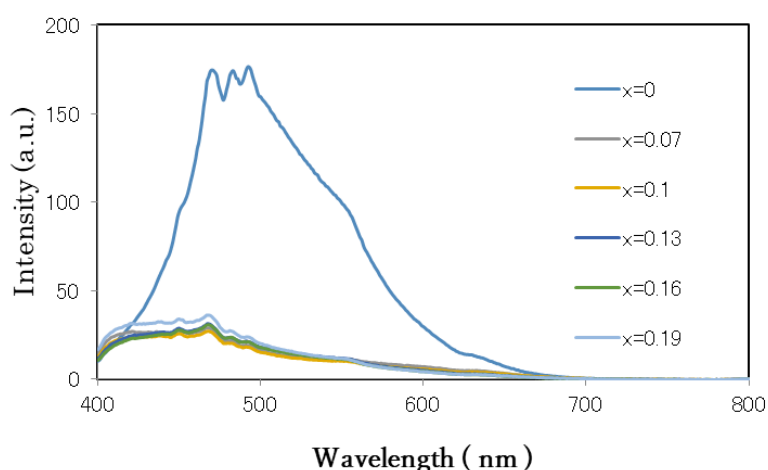


**Figure 5.** Photoluminescence spectra for  $\text{Zn}_{(1-2x)}(\text{CuGa})_x\text{In}_2\text{S}_4$  excitation: 350 nm.

### 3.4. Photocatalytic Activity

A hydrogen generation was conducted using the photocatalyst  $\text{Zn}_{(1-2x)}(\text{CuGa})_x\text{In}_2\text{S}_4$ .  $\text{ZnIn}_2\text{S}_4$ ,  $\text{Zn}_{0.87}\text{Cu}_{0.13}\text{In}_2\text{S}_{3.935}$ , and  $\text{Zn}_{0.87}\text{Ga}_{0.13}\text{In}_2\text{S}_{4.065}$  were used as comparative objects. All catalysts were

loaded with 1 wt% Pt as a cocatalyst. The results are shown in Figure S5. The photocatalyst mono-doped with Ga or Cu showed higher hydrogen generation activity than pure  $\text{ZnIn}_2\text{S}_4$ . Furthermore, the photocatalyst co-doped with Cu and Ga showed the highest hydrogen generation activity. The optimum doping amounts of Cu and Ga were investigated, as shown in Figure 6.

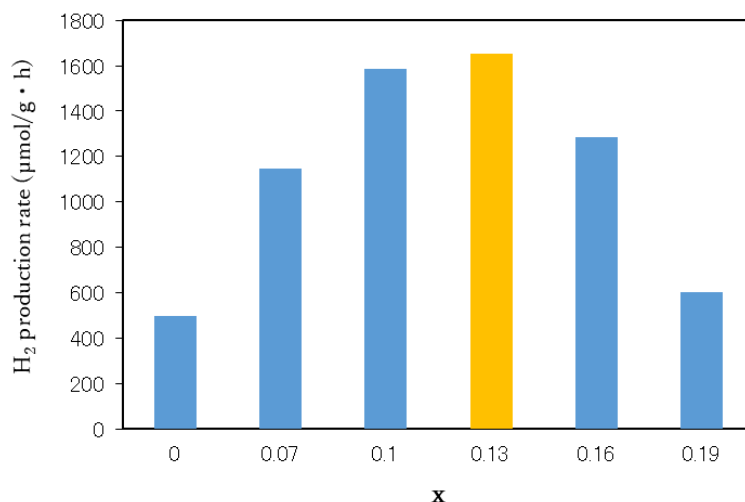


**Figure 6.** Photocatalytic hydrogen production rate with  $\text{Zn}_{(1-2x)}(\text{CuGa})_x\text{In}_2\text{S}_4$ .

The hydrogen generation increased when the doping amount of Cu and Ga was from  $x = 0$  to 0.13. The largest  $\text{H}_2$  production rate was obtained with  $\text{Zn}_{(1-2x)}(\text{CuGa})_x\text{In}_2\text{S}_4$  ( $x = 0.13$ ), and it was 3.3 times better than that of  $\text{ZnIn}_2\text{S}_4$ . However, the amount of hydrogen decreased from  $x = 0.16$  to 0.19. The reason for the photocatalytic activity from increase to decrease may be due to the shielding by Cu and Ga. The dependence of photocatalytic  $\text{H}_2$  generation on doping levels has been reported by other studies [31,37]. In the stability test of the photocatalyst in Figure 7, The decrease in the amount of hydrogen production could not be observed in four cycles. A slight change in the amount of hydrogen produced in the 3rd and 4th cycles may have been due to the deterioration of the sacrificial agent. The TEM images before and after the hydrogen generation of  $\text{Zn}_{(1-2x)}(\text{CuGa})_x\text{In}_2\text{S}_4$  photocatalyst are shown in the Figure S6. Only after hydrogen generation, a 3–4 nm spot was observed on the sample surface. The spot deposition was Pt, which was produced by the reduction during the hydrogen production.

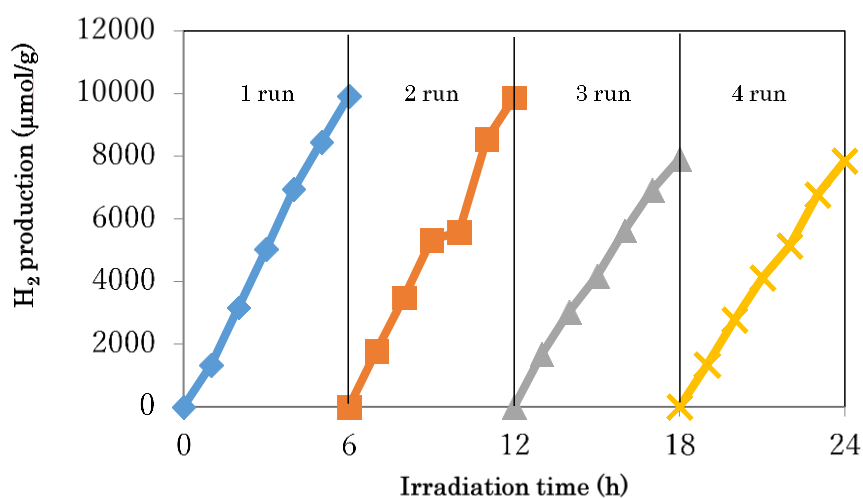
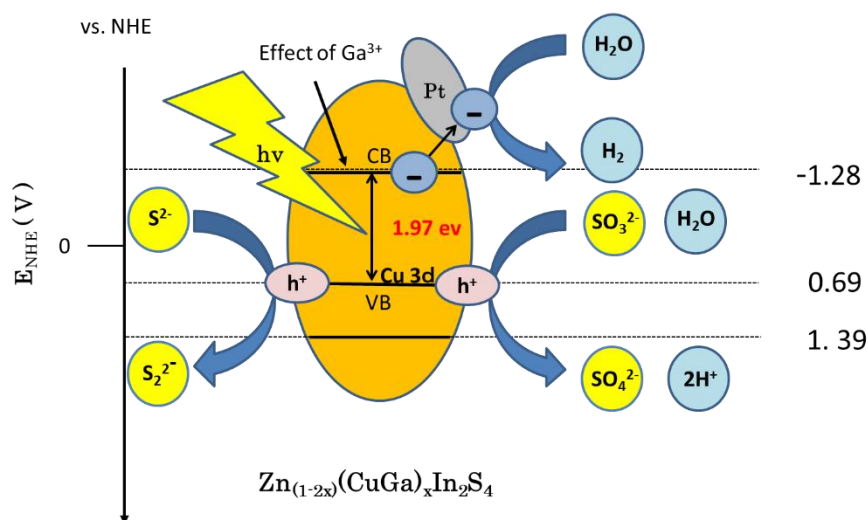
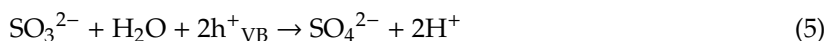


**Figure 7.** Cycling runs of  $\text{Zn}_{0.74}(\text{CuGa})_{0.13}\text{In}_2\text{S}_4$ .

### 3.5. Proposed Hydrogenation Mechanism

The reaction mechanism is shown in Scheme 1. Irradiation of light having a wavelength corresponding to the band gap energy of the  $Zn_{(1-2x)}(CuGa)_xIn_2S_4$  photocatalyst excites electrons in the valence band of  $Zn_{(1-2x)}(CuGa)_xIn_2S_4$  to the conduction band, in order to produce an electron hole pair (Equation (2)). The band gap in the case of  $Cu^+$  and  $Ga^{3+}$  co-doping was narrowed by forming impurity levels derived from the Cu 3d and Ga 4s orbitals on the negative side of the valence band and the positive side of the conduction band of  $ZnIn_2S_4$ , respectively. The tuned band gap promotes charge separation of the photocatalyst and improves the visible light response. In Equation (3), some of electrons excited in the conduction band of  $Zn_{(1-2x)}(CuGa)_xIn_2S_4$  are consumed for the photodeposition of Pt. The hydrogen was produced from  $H_2O$  and electrons which were transferred from conduction band of  $Zn_{(1-2x)}(CuGa)_xIn_2S_4$  to Pt metal (Equation (4)). On the other hand, with regard to holes, sulfite ions and sulfide ions consume the holes and promote a hydrogen generation reaction. The presence of  $Na_2S$  is very important for enhancing the photocatalytic activity; on the other hand,  $Na_2S$  stabilizes the surface of the metal sulfide by suppressing the formation of surface defects as a scavenger of holes. However, when the concentration of  $Na_2S$  is high, the pH becomes high. High pH values are thermodynamically disadvantageous in the reaction represented by Equation (4). As described in the Equations (5)–(7),  $SO_3^{2-}$  and  $S^{2-}$  consume holes, and promote hydrogen generation reaction. According to Equation (6),  $S_2^{2-}$  ions are generated and act as an optical filter. If  $S_2^{2-}$  is not consumed, it interferes with light absorption. As shown in Equation (8), the reaction between  $S_2^{2-}$  and  $SO_3^{2-}$  forms  $S_2O_3^{2-}$ , is colorless and does not compete with light absorption.



Scheme 1.  $H_2$  production mechanism.

#### 4. Conclusions

The novel  $Zn_{(1-2x)}(CuGa)_xIn_2S_4$  photocatalyst, in which  $ZnIn_2S_4$  is co-doped with  $Cu^+$  and  $Ga^{3+}$  was prepared by a simple one-pot solvothermal method. The amount of doping with  $Cu^+$  and/or  $Ga^{3+}$  into  $ZnIn_2S_4$  has effects on the crystal structures, morphologies, optical properties, and photocatalytic activities of the obtained  $Zn_{(1-2x)}(CuGa)_xIn_2S_4$  photocatalysts. From the SEM image, doping  $Cu^+$  and  $Ga^{3+}$  breaks microsphere-like flowers. That is due to the insertion of  $Cu^+$  and  $Ga^{3+}$  into  $Zn^{2+}$  parts of  $ZnIn_2S_4$ . A shifted XRD pattern showed that  $Zn_{(1-2x)}(CuGa)_xIn_2S_4$  has a high probability for a solid solution of having a hexagonal  $ZnIn_2S_4$  as its basic structure. XPS spectra suggests the presence of  $Cu^+$  and  $Ga^{3+}$  in  $Zn_{(1-2x)}(CuGa)_xIn_2S_4$ . DRS and PL results show that the control of the band gap and suppression of electron-hole recombination were confirmed by doping  $ZnIn_2S_4$  with  $Cu^+$  and  $Ga^{3+}$ . In addition, the doping of  $Cu^+$  and  $Ga^{3+}$  improved the photocatalytic activity. The optimum doping amount was Zn: (CuGa) = 0.74:0.13. The hydrogen generation rate by  $Zn_{(1-2x)}(CuGa)_xIn_2S_4$  at the optimum doping amount was  $1650 \mu\text{mol}\cdot\text{g}^{-1}\cdot\text{h}^{-1}$ , which was 3.3 times higher than that of  $ZnIn_2S_4$  ( $500 \mu\text{mol}\cdot\text{g}^{-1}\cdot\text{h}^{-1}$ ). Furthermore, this photocatalyst showed good stability during 24 h of hydrogen generation.

**Supplementary Materials:** The following are available online at <http://www.mdpi.com/2305-7084/3/4/79/s1>: Table S1: Starting material for the preparation of photocatalyst; Table S2: Expected composite components of photocatalyst (molar ratio); Table S3: Elemental ratios of  $Zn_{(1-2x)}(CuGa)_xIn_2S_4$  from XPS result; Table S4: Surface area of photocatalysts; Figure S1: XPS survey spectra of  $Zn_{(1-2x)}(CuGa)_xIn_2S_4$ ; Figure S2: Adsorption/desorption Isotherm of  $Zn_{(1-2x)}(CuGa)_xIn_2S_4$ ; Figure S3: Tauc plots of  $Zn_{(1-2x)}(CuGa)_xIn_2S_4$ ; Figure S4: Valence-band edge XPS spectra of (a)  $ZnIn_2S_4$ , (b)  $Zn_{0.74}(CuGa)_{0.13}In_2S_4$ . Figure S5: Photocatalytic hydrogen production with (a)  $ZnIn_2S_4$  (rhombus), (b)  $Zn_{0.87}Ga_{0.13}In_2S_{4.065}$  (cross), (c)  $Zn_{0.87}Cu_{0.13}In_2S_{3.935}$  (triangle), and (d)  $Zn_{0.74}(CuGa)_{0.13}In_2S_4$  (square). Pt doping: 1.0 wt%. Figure S6: TEM images of  $Zn_{0.74}(CuGa)_{0.13}In_2S_4$ .

**Author Contributions:** I.T. and H.K. conceived and designed the experiments. I.T. performed the experiments and wrote the paper. I.T., M.F., S.K., and H.K. analyzed the results and advised the project.

**Conflicts of Interest:** The authors declare no conflict of interest.

**Note:** All experiments were conducted at Mie University. Any opinions, findings, conclusions or recommendations expressed in this paper are those of the authors and do not necessarily reflect the view of the supporting organizations.

#### References

1. Kudo, A. Development of photocatalyst materials for water splitting. *Int. J. Hydrogen Energy* **2006**, *31*, 197–202. [[CrossRef](#)]
2. Kato, H.; Kudo, A. Photocatalytic water splitting into  $H_2$  and  $O_2$  over various tantalate photocatalysts. *Catal. Today* **2003**, *78*, 561–569. [[CrossRef](#)]
3. Chen, X.; Shen, S.; Guo, L.; Mao, S.S. Semiconductor-based Photocatalytic Hydrogen Generation. *Chem. Rev.* **2010**, *110*, 6503–6570. [[CrossRef](#)] [[PubMed](#)]
4. Sorcar, S.; Hwang, Y.; Lee, J.; Kim, H.; Grimes, K.M.; Grimes, C.A.; Jung, J.-W.; Cho, C.-H.; Majima, T.; Hoffmann, M.R.; et al.  $CO_2$ , water, and sunlight to hydrocarbon fuels: A sustained sunlight to fuel (Joule-to-Joule) photoconversion efficiency of 1%. *Energy Environ. Sci.* **2019**, *12*, 2685–2696. [[CrossRef](#)]
5. Schreier, M.; Héroguel, F.; Steier, L.; Ahmad, S.; Luterbacher, J.S.; Mayer, M.T.; Luo, J.; Grätzel, M. Solar conversion of  $CO_2$  to CO using Earth-abundant electrocatalysts prepared by atomic layer modification of CuO. *Nat. Energy* **2017**, *2*, 17087. [[CrossRef](#)]
6. Kumar, B.; Asadi, M.; Pisasale, D.; Ray, S.S.; Rosen, B.A.; Haasch, R.; Abiade, J.; Yarin, A.L.; Khojin, A.S. Renewable and metal-free carbon nanofiber catalysts for carbon dioxide reduction. *Nat. Commun.* **2013**, *4*, 2819. [[CrossRef](#)]
7. Tsuji, I.; Kato, H.; Kobayashi, H.; Kudo, A. Photocatalytic  $H_2$  evolution reaction from aqueous solutions over band structure-controlled  $(AgIn)_xZn_{2(1-x)}S_2$  solid solution photocatalysts with visible-light response and their surface nanostructures. *J. Am. Chem. Soc.* **2004**, *126*, 13406–13413. [[CrossRef](#)] [[PubMed](#)]
8. Peng, S.; Zhu, P.; Thavasi, V.; Mhaisalkar, S.G.; Ramakrishna, S. Facile solution deposition of  $ZnIn_2S_4$  nanosheet films on FTO substrates for photoelectric application. *Nanoscale* **2011**, *3*, 2602–2608. [[CrossRef](#)]

9. Zhang, X.; Yu, L.; Zhuang, C.; Peng, T.; Li, R.; Li, X. Highly Asymmetric Phthalocyanine as a Sensitizer of Graphitic Carbon Nitride for Extremely Efficient Photocatalytic H<sub>2</sub> Production under Near-Infrared Light. *ACS Catal.* **2014**, *4*, 162–170. [[CrossRef](#)]
10. Dai, W.W.; Zhao, Z.Y. DFT study on the interfacial properties of vertical and in-plane BiOI/BiOIO<sub>3</sub> hetero-structures. *Phys. Chem. Chem. Phys.* **2017**, *19*, 9900–9911. [[CrossRef](#)] [[PubMed](#)]
11. Vaiano, V.; Iervolino, G.; Rizzo, L. Cu-doped ZnO as efficient photocatalyst for the oxidation of arsenite to arsenate under visible light. *Appl. Catal. B* **2018**, *238*, 471–479. [[CrossRef](#)]
12. Shafae, M.; Goharshadi, E.K.; Mashreghi, M.; Sadeghinia, M. TiO<sub>2</sub> nanoparticles and TiO<sub>2</sub>@graphene quantum dots nanocomposites as effective visible/solar light photocatalysts. *J. Photochem. Photobiol. A Chem.* **2018**, *357*, 90–102. [[CrossRef](#)]
13. Chang, C.J.; Wang, C.W.; Wei, Y.H.; Chen, C.Y. Enhanced photocatalytic H<sub>2</sub> production activity of Ag-doped Bi<sub>2</sub>WO<sub>6</sub>-graphene based photocatalysts. *Int. J. Hydrogen Energy* **2018**, *43*, 11345–11354. [[CrossRef](#)]
14. Jia, Y.; Zhao, D.; Li, M.; Han, H.; Li, C. La and Cr Co-doped SrTiO<sub>3</sub> as an H<sub>2</sub> evolution photocatalyst for construction of a Z-scheme overall water splitting system. *Chin. J. Catal.* **2018**, *39*, 421–430. [[CrossRef](#)]
15. Yan, X.; Xue, C.; Yang, B.; Yang, G. Novel three-dimensionally ordered macroporous Fe<sup>3+</sup>-doped TiO<sub>2</sub> photocatalysts for H<sub>2</sub> production and degradation applications. *Appl. Surf. Sci.* **2017**, *394*, 248–257. [[CrossRef](#)]
16. Singh, J.; Sharma, S.; Sharma, S.; Singh, R.C. Effect of tungsten doping on structural and optical properties of rutile TiO<sub>2</sub> and band gap narrowing. *Optik* **2019**, *182*, 538–547. [[CrossRef](#)]
17. Sharma, P.K.; Cortes, M.A.L.; Hamilton, J.W.; Han, Y.; Byrne, J.A.; Nolan, M. Surface modification of TiO<sub>2</sub> with copper clusters for band gap narrowing. *Catal. Today* **2018**, *321–322*, 9–17. [[CrossRef](#)]
18. Liu, C.; Chai, B.; Wang, C.; Yan, J.; Ren, Z. Solvothermal fabrication of MoS<sub>2</sub> anchored on ZnIn<sub>2</sub>S<sub>4</sub> microspheres with boosted photocatalytic hydrogen evolution activity. *Int. J. Hydrogen Energy* **2018**, *43*, 6977–6986. [[CrossRef](#)]
19. Gao, P.; Li, A.; Sun, D.D.; Ng, W.J. Effects of various TiO<sub>2</sub> nanostructures and graphene oxide on photocatalytic activity of TiO<sub>2</sub>. *J. Hazard. Mater.* **2014**, *279*, 96–104. [[CrossRef](#)] [[PubMed](#)]
20. Guo, J.; Liao, X.; Lee, M.-H.; Hyett, G.; Huang, C.C.; Hewak, D.W.; Mails, S.; Zhou, W.; Jiang, Z. Experimental and DFT insights of the Zn-doping effects on the visible-light photocatalytic water splitting and dye decomposition over Zn-doped BiOBr photocatalysts. *Appl. Catal. B* **2019**, *243*, 502–512. [[CrossRef](#)]
21. Behzadifard, Z.; Shariatnia, Z.; Jourshabani, M. Novel visible light driven CuO/SmFeO<sub>3</sub> nanocomposite photocatalysts with enhanced photocatalytic activities for degradation of organic pollutants. *J. Mol. Liq.* **2018**, *262*, 533–548. [[CrossRef](#)]
22. Li, T.L.; Cai, C.D.; Yeh, T.F.; Teng, H. Capped CuInS<sub>2</sub> quantum dots for H<sub>2</sub> evolution from water under visible light illumination. *J. Alloys Compd.* **2013**, *550*, 326–330. [[CrossRef](#)]
23. You, D.; Pan, B.; Jiang, F.; Zhou, Y.; Su, W. CdS nanoparticles/CeO<sub>2</sub> nanorods composite with high-efficiency visible-light-driven photocatalytic activity. *Appl. Surf. Sci.* **2016**, *363*, 154–160. [[CrossRef](#)]
24. Jin, X.; Chen, F.; Jia, D.; Cao, Y.; Duan, H.; Long, M.; Yang, L. Influences of synthetic conditions on the photocatalytic performance of ZnS/graphene composites. *J. Alloys Compd.* **2019**, *780*, 299–305. [[CrossRef](#)]
25. Zhang, S.; Wang, L.; Liu, C.; Luo, J.; Crittenden, J.; Liu, X.; Ca, T.; Yuan, J.; Pei, Y.; Liu, Y. Photocatalytic wastewater purification with simultaneous hydrogen production using MoS<sub>2</sub> QD-decorated hierarchical assembly of ZnIn<sub>2</sub>S<sub>4</sub> on reduced graphene oxide photocatalyst. *Water Res.* **2017**, *121*, 11–19. [[CrossRef](#)] [[PubMed](#)]
26. Fan, B.; Chen, Z.H.; Liu, Q.; Zhang, Z.G.; Fang, X.M. One-pot hydrothermal synthesis of Ni-doped ZnIn<sub>2</sub>S<sub>4</sub> nanostructured film photoelectrodes with enhanced photoelectrochemical performance. *Appl. Surf. Sci.* **2016**, *370*, 252–259. [[CrossRef](#)]
27. Ding, Y.; Gao, Y.; Li, Z. Carbon quantum dots (CQDs) and Co(dmgh)<sub>2</sub>PyCl synergistically promote photocatalytic hydrogen evolution over hexagonal ZnIn<sub>2</sub>S<sub>4</sub>. *Appl. Surf. Sci.* **2018**, *462*, 255–262. [[CrossRef](#)]
28. Zeng, C.; Huang, H.; Zhang, T.; Dong, F.; Zhang, Y.; Hu, Y. Fabrication of Heterogeneous-Phase Solid-Solution Promoting Band Structure and Charge Separation for Enhancing Photocatalytic CO<sub>2</sub> Reduction: A Case of Zn<sub>x</sub>Ca<sub>1-x</sub>In<sub>2</sub>S<sub>4</sub>. *ACS Appl. Mater. Interfaces* **2017**, *9*, 27773–27783. [[CrossRef](#)]
29. Sun, M.; Zhao, X.; Zeng, Q.; Yan, T.; Ji, P.G.; Wu, T.T.; Wei, D.; Du, B. Facile synthesis of hierarchical ZnIn<sub>2</sub>S<sub>4</sub>/CdIn<sub>2</sub>S<sub>4</sub> microspheres with enhanced visible light driven photocatalytic activity. *Appl. Surf. Sci.* **2017**, *407*, 328–336. [[CrossRef](#)]

30. Liu, A.; Yu, C.; Lin, J.; Sun, G.; Xu, G.; Huang, Y.; Liu, Z.; Tang, C. Construction of CuInS<sub>2</sub>@ZIF-8 nanocomposites with enhanced photocatalytic activity and durability. *Mater. Res. Bull.* **2019**, *112*, 147–153. [[CrossRef](#)]
31. Shen, S.; Zhao, L.; Zhou, Z.; Guo, L. Enhanced Photocatalytic Hydrogen Evolution over Cu-Doped ZnIn<sub>2</sub>S<sub>4</sub> under Visible Light Irradiation. *J. Phys. Chem. C* **2008**, *112*, 16148–16155. [[CrossRef](#)]
32. Zhang, G.; Zhang, W.; John, C.C.; Chen, Y.; Minakata, D.; Wang, P. Photocatalytic hydrogen production under visible-light irradiation on (CuAg)<sub>0.15</sub>In<sub>0.3</sub>Zn<sub>1.4</sub>S<sub>2</sub> synthesized by precipitation and calcination. *Chin. J. Catal.* **2013**, *34*, 1926–1935. [[CrossRef](#)]
33. Liu, X.; Khan, M.; Liu, W.; Xiang, W.; Guan, M.; Jiang, P.; Cao, W. Synthesis of nanocrystalline Ga–TiO<sub>2</sub> powders by mild hydrothermal method and their visible light photoactivity. *Ceram. Int.* **2015**, *41*, 3075–3080. [[CrossRef](#)]
34. Khallaf, H.; Chai, G.; Lupan, O.; Chow, C.; Park, S.; Schulte, A. Characterization of gallium-doped CdS thin films grown by chemical bath deposition. *Appl. Surf. Sci.* **2009**, *255*, 4129–4134. [[CrossRef](#)]
35. Sola, A.C.; Gösser, M.B.; de la Piscina, P.R.; Homs, N. Promoter effect of Ga in Pt/Ga-TiO<sub>2</sub> catalysts for the photo-production of H<sub>2</sub> from aqueous solutions of ethanol. *Catal. Today* **2017**, *287*, 85–90. [[CrossRef](#)]
36. Da Costa, R.C.; Rodrigues, A.D.; Pizani, P.S. Phase mixture, solid solution or composite: Raman scattering analyses of Ni<sub>x</sub>Pb<sub>1-x</sub>TiO<sub>3</sub> and (NiTiO<sub>3</sub>)<sub>x</sub>(PbTiO<sub>3</sub>)<sub>1-x</sub>. *J. Alloys Compd.* **2017**, *697*, 68–71. [[CrossRef](#)]
37. Kaga, H.; Kudo, A. Cosubstituting effects of copper(I) and gallium(III) for ZnGa<sub>2</sub>S<sub>4</sub> with defect chalcopyrite structure on photocatalytic activity for hydrogen evolution. *J. Catal.* **2014**, *310*, 31–36.
38. Chai, B.; Liu, C.; Wang, C.; Yan, J.; Ren, Z. Photocatalytic hydrogen evolution activity over MoS<sub>2</sub>/ZnIn<sub>2</sub>S<sub>4</sub> microspheres. *Chin. J. Catal.* **2017**, *38*, 2067–2075. [[CrossRef](#)]
39. Cui, W.; Guo, D.; Liu, L.; Hu, J.; Rana, D.; Liang, Y. Preparation of ZnIn<sub>2</sub>S<sub>4</sub>/K<sub>2</sub>La<sub>2</sub>Ti<sub>3</sub>O<sub>10</sub> composites and their photocatalytic H<sub>2</sub> evolution from aqueous Na<sub>2</sub>S/Na<sub>2</sub>SO<sub>3</sub> under visible light irradiation. *Catal. Commun.* **2014**, *48*, 55–59. [[CrossRef](#)]
40. Du, C.; Zhang, Q.; Lin, Z.; Yan, B.; Xia, C.; Yang, G. Half-unit-cell ZnIn<sub>2</sub>S<sub>4</sub> monolayer with sulfur vacancies for photocatalytic hydrogen evolution. *Appl. Catal. B* **2019**, *248*, 193–201. [[CrossRef](#)]
41. Yang, X.; Li, Q.; Lv, K.L.; Li, M. Heterojunction construction between TiO<sub>2</sub> hollowsphere and ZnIn<sub>2</sub>S<sub>4</sub> flower for photocatalysis application. *Appl. Surf. Sci.* **2017**, *398*, 81–88.
42. Yue, W.; Han, S.; Peng, R.; Shen, W.; Geng, H.; Wu, F.; Tao, S.; Wang, M. CuInS<sub>2</sub> quantum dots synthesized by a solvothermal route and their application as effective electron acceptors for hybrid solar cells. *J. Mater. Chem.* **2010**, *20*, 7570–7578. [[CrossRef](#)]
43. Sudip, K.B.; Tian, L.; Venkatram, N.; Wei, J.; Vittal, J.J. Phase-selective synthesis of CuInS<sub>2</sub> nanocrystals. *J. Phys. Chem. C* **2009**, *113*, 15037–15042.
44. Zepeda, T.A.; Pawelec, B.; De Leon, J.D.; De los Reyes, J.A.; Olivas, A. Effect of gallium loading on the hydrodesulfurization activity of unsupported Ga<sub>2</sub>S<sub>3</sub>/WS<sub>2</sub> catalysts. *Appl. Catal. B* **2012**, *111–112*, 10–19. [[CrossRef](#)]
45. Chen, S.; Li, S.; Xiong, L.; Wang, G. In-situ growth of ZnIn<sub>2</sub>S<sub>4</sub> decorated on electrospun TiO<sub>2</sub> nanofibers with enhanced visible-light photocatalytic activity. *Chem. Phys. Lett.* **2018**, *706*, 68–75. [[CrossRef](#)]

